Experimental realization of on-chip surface acoustic wave metasurfaces at sub-GHz

Wan Wang[1,2], Maciej Baranski[2], Yabin Jin[3,4,*], Roland Salut[2], Djaffar Belharet[2], Jean-Michel Friedt[2], Yongdong Pan[1], Yanxun Xiang[3], Fu-zhen Xuan[3], Abdelkrim Khelif[2], Sarah Benchabane[2,*]

[1]School of Aerospace Engineering and Applied Mechanics, Tongji University, 200092 Shanghai, China

[2]Université de Franche-Comté, CNRS, FEMTO-ST, 15B avenue des Montboucons F-25000 Besançon, France

[3]Shanghai Key Laboratory of Intelligent Sensing and Detection Technology, School of Mechanical and Power Engineering, East China University of Science and Technology, 200237 Shanghai, China

[4]Shanghai Institute of Aircraft Mechanics and Control, 200092 Shanghai, China

*Corresponding author: yabin.jin@ecust.edu.cn; sarah.benchabane@femto-st.fr

Metasurfaces, consisting of subwavelength-thickness units with different wave responses, provide an innovative possible method to manipulate elastic and acoustic waves efficiently. The application of metasurfaces to manipulate on-chip surface acoustic wave (SAW) at sub-giga frequencies requires further exploration since their wave functions are highly demanded in nanoelectromechanical systems (NEMS), sensing, communications, microfluid control and quantum processing. Here, we report the experimental realization of on-chip SAW metasurfaces, consisting of gradient submicron niobium (Nb) rectangular pillars positioned on a 128°Y-cut lithium niobate (LiNbO$_3$) substrate that operate at hundreds of megahertz. The proposed SAW metasurfaces are able to manipulate transmitted SAW wavefront functions by designing on-demand pillar's profile distributions. We experimentally demonstrate broadband subwavelength focusing effects as the typical functions of SAW metasurfaces. This study opens a door for realizing on-chip SAW metasurfaces for diverse potential applications at micro- and nanoscale.

1. Introduction

The concept of metasurfaces, as illustrated in Fig. 1a, comprising subwavelength-thickness units with nonhomogeneous phase response, offers a novel approach to efficiently manipulate wave phenomena. Compared with metamaterials [1, 2] and phononic crystals [3, 4], whose overall thickness typically exceeds several wavelengths (Fig. 1b), metasurfaces offer significant advantages due to their compact size, aligning with the highly integrated nature of modern chips and the imperative to mitigate power cost and minimize cross-talk. Recently, metasurfaces have rapidly evolved in optical waves [5-7], microwaves [8, 9], acoustic waves [10-12], and extended to mechanical system [13], with numerous intriguing functionalities proposed, such as focusing [14-16], source illusion [17], or total internal reflection[18]. Various designs have been proposed to control the elastic waves, including space curl structure[17], tailored structure[19] and resonant

pillar [20]. Most research focused on macro-scale structures and plate-type or bulk media, however, their complex structures make it difficult to be applied to submicron or nanoscale. This limitation hinders the practical application of elastic metasurfaces particularly in quantum chips and communication science [21].
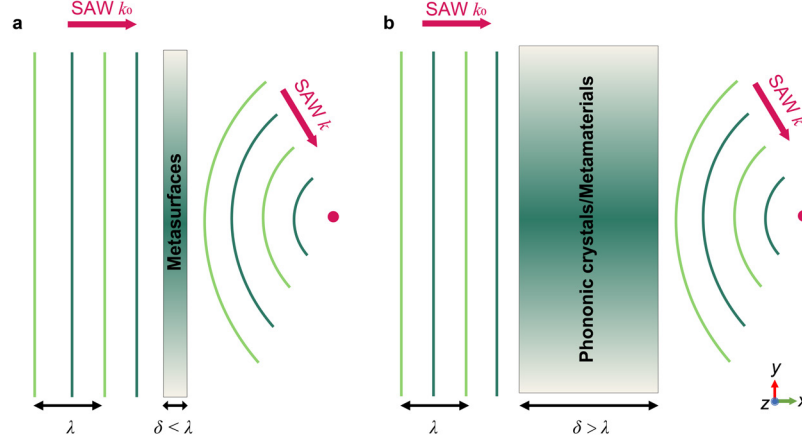
Fig.1 Illustration of **(a)** metasurfaces and **(b)** phononic crystals/metamaterials. δ represents the total thickness of metasurface or phononic crystals/metamaterials, while λ denotes the SAW wavelength.

Surface acoustic waves (SAW), serving as an excellent platform for working with high-frequency signals, have garnered significant attention since the last century. SAW devices are widely utilized in current RF industries, such as filter, delay line, resonators and microfluid chips. In recent years, numerous new promising applications of SAW have been proposed, spanning classical sensing [22, 23], actuation [24, 25], and quantum science [26, 27], highlighting an urgent demand for arbitrary design of SAW wavefronts at micro-nano scale. The control of chip-scale SAW has typically been achieved using electrical electrodes. Due to their advantages in ease of manufacturing through microfabrication, interdigital transducers (IDTs) consist of arrays of metallic electrodes are commonly used not only to excite plane SAW [28], but also to obtain focused SAW [29, 30]. However, given the active properties and electromechanical coupling mechanisms, the focused IDTs limits the efficient SAW generations and broad-field focusing within the chip. The dislocated interdigital transducer [31], as a type of phased array active structure, offers a better solution to mitigate the electromechanical coupling efficiency compared to the focused IDT. While electrode generators offer real-time tunability and broad control flexibility, mechanical and passive components provide different advantages for within-chip control, especially in enabling complex out-of-source modulation.

Besides the active solutions mentioned above, SAW modulation can be effectively achieved using artificially structured materials like phononic crystals amd metamaterials. By incorporating line defects, phononic crystals enable micro-scale SAW waveguides with functionalities such as splitting and bending [32], while the integration of topological concepts allows for the design of robust waveguides [33]. Acoustic lenses can be realized either through the anisotropic propagation

characteristics of tungsten/lithium niobate phononic crystals [34] or by employing gradient-index phononic crystal [35, 36]. Moreover, metamaterials provide a means to achieve SAW attenuation [37, 38], extending the range of functionalities offered by structured materials. Although phononic crystals/metamaterials offer diverse functionalities, subwavelength metasurfaces present a superior choice for controlling SAW as menthioned at the begining. Screw-nut structures are also employed for wavefront modulation of Rayleigh waves around 40kHz [39]. Sub-wavelength resonant mass-spring microstructures are used to achieve local acoustic field gradients at 7 MHz[40]. Sawtooth-based metasurfaces leveraging diffractive effects are proposed for flexibly steering acoustic fields in microfluidic device around 40 MHz [41]. Such subwavelength metassurfaces provide a new efficient way in SAW microfluidics[42]. However, how to achieve SAW subwavelength metasurfaces at higher frequencies such as sub-giga Hertz remains challenging.

To address the aforementioned challenges, we propose a new approach to realize on-chip SAW metasurface. Due to the significant advantages of the pillar-based platform [43, 44] in microfabrication, we design the metasurface unit consisting of a series of identical pillars to enhance their resonant modes which can generate efficient phase shift and high amplitude for transmitted SAWs. We further investigate mechanisms for efficient phase modulation by analyzing the scattering property of pillar's resonant modes and the interference between the scattered and incident SAWs. By designing varied width and thickness of rectangular pillars in metasurface units, the on-chip SAW metasurfaces are able to manipulate wavefront shaping of the transmitted SAWs. We present the design methodology for broadband subwavelength focusing effect as an example of wave functions [45, 46]. A microfabrication process including E-beam lithography and plasma etching is utilized for sample preparation. The capability for broadband focusing is emphasized through both simulations and experiments to validate the proposed on-chip SAW metasurfaces which have potential applications at micro- and nanoscale for NEMS, sensing, communications, quantum processing, among others.

2. Metasurface units design

The key in designing an efficient metasurface lies in obtaining a 2π span of the transmitted phase alongside high amplitude. Unlike Lamb waves, introducing a single resonating pillar acting as a point source for SAW modulation proves challenging due to the radiation into the bulk of the piezoelectric substrate. In the study of on-chip SAW metasurface units, we investigate the response of a group of resonating pillars under SAW excitation. The SAW metasurface unit consists of several identical niobium (Nb) rectangular pillars positioned on a 128°Y-cut lithium niobate (LiNbO₃) substrate, as illustrated in Fig. 2a. The Young's modulus of niobium is 105.3 GPa, with a Poisson's ratio of 0.39 and a density of 8571.3 kg/m³. The continuity condition is applied to both sides along the y-axis direction to simulate an infinite structure and avoid boundary effects. Additionally, Perfectly Matched Layer (PML) surrounding the model is employed to minimize reflections from the boundaries. SAW is launched along x direction by vertical force excitation, and the transmitted waves are subsequently detected on the other side of substrate surface. More details about the numerical simulations can be found in Supplymentary Materials.

The first step in unit design is to choose the optimal number of pillars. We set the lattice constant $a = 1.5$ μm, the height of pillars $h = 0.45$ μm, interval between two pillars $d = 0.6$ μm, thickness of pillar $t = 0.5$ μm, width of pillar $w = 0.914$ μm and working frequency $f = 600$ MHz, corresponding to a simulated wavelength $\lambda = 6.7$ μm. These geometrical parameters are obtained through a broad search and correspond to a specific resonance state, which will be described later. The resonant pillar acts as a secondary excitation source, stimulating the scattered wave; and the resulting transmitted wave emerges from the destructive interference between the incident wave and the scattered wave [47]. To delve deeper into the working mechanisms of metasurface units, a scattering field analysis was conducted. The scattering field can be derived by subtracting the out-of-plane displacement field in the presence of the pillars from that without them.
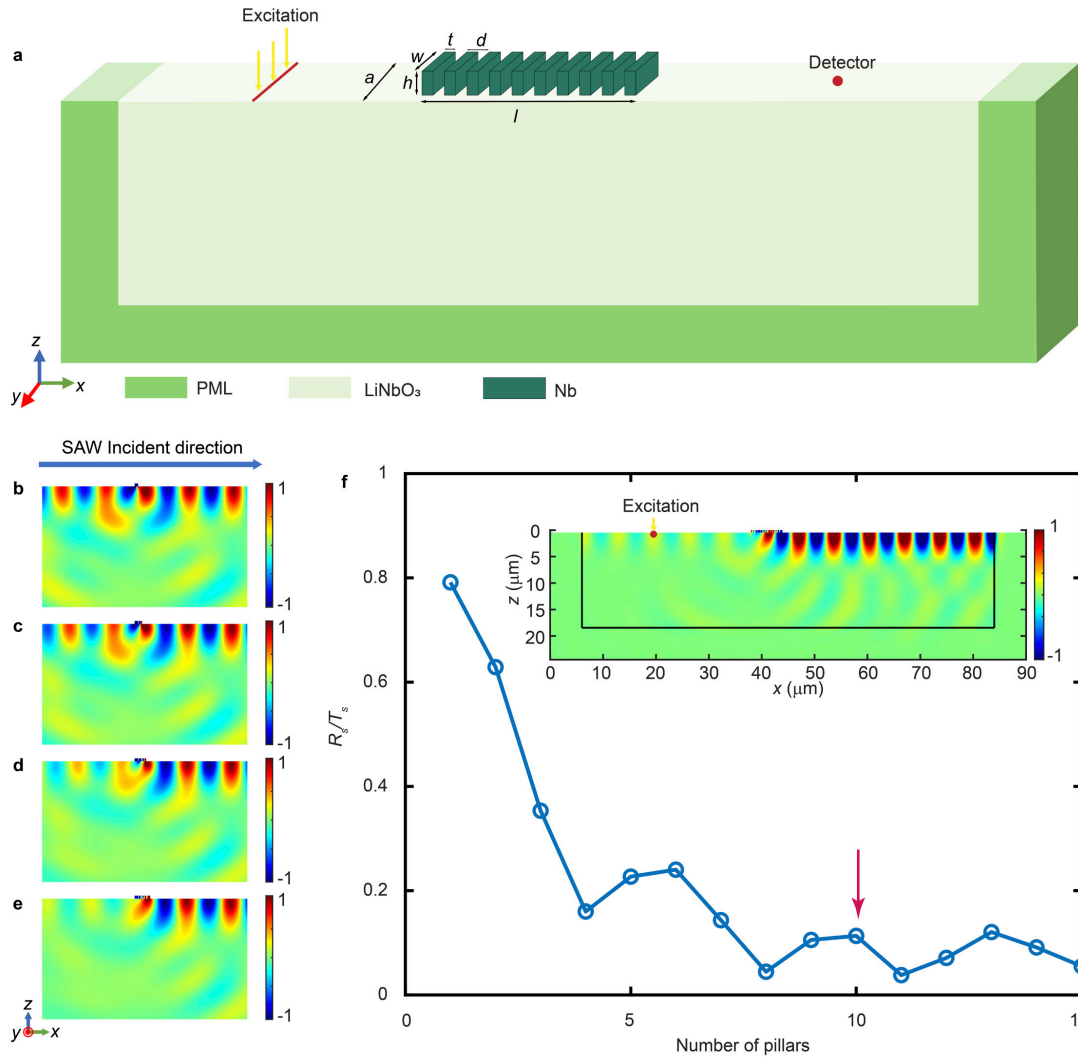

Fig.2 a, Illustration of the metasurface units. **(b)~ (e)** show the scattering fields of metasurface units with 1 to 4 pillars, respectively. **f,** variation of R_s/T_s as a function of the number of pillars, where R_s represents the amplitude of reflected scattering wave and T_s represents the amplitude of transmitted scattering wave; Inset is the scattering field with 10 pillars.

In Fig.2b to 2e, we present the scattering fields for pillar numbers ranging from 1 to 4, respectively. It can be observed that when there is only a single bending-resonance pillar, it behaves like a dipolar point source, with its transmitted and reflected scattered fields being of comparable strength, as shown in Fig.2b. As the number of pillars increases, their reflected scattering waves exhibit destructive interference, while the transmitted scattering waves demonstrate constructive interference. This can lead to a reduction of reflected energy and a corresponding increase in transmission efficiency. To make this change more intuitively demonstrable, we define a coefficient R_s/T_s, where R_s represents the amplitude of reflected scattering wave and T_s represents the amplitude of transmitted scattering wave. A ratio of 1 indicates a similar intensity of reflected and transmitted scattering, while a ratio close to 0 signifies almost no reflection, achieving full transmission. Fig.2f illustrates the relationship between R_s/T_s and the number of pillars. It is evident that further increasing the number of pillars results in negligible gains in transmittance efficiency while significantly enlarging the size, thereby diminishing the compactness advantage of metasurfaces. Considering the balance between efficiency and the overall dimensions of the structure, a 10-pillar configuration is chosen as the metasurface unit, and its scattering field is shown in the inset of Fig. 2f. With such geometric size and operating frequency, the total length l of the proposed metasurface is approximately 6 μm, less than one wavelength. As a side note, the results for transmitted waves (a combination of incident and scattering waves) can be found in the Supplementary Materials.

To achieve 2π phase variation, the thickness t and width w of pillars can be adjusted to introduce different resonance states of the unit. These parameters were primarily chosen to align with the 2D patterning preferences and precision limitations of standard microfabrication techniques. The transmitted phase and amplitude transmission are defined as the ratio of the out-of-plane displacement of the transmitted wave (with pillars) to that of the incident wave (without pillars). By varying the width (from 0.1 μm to 1.4 μm) and thickness (from 0.1 μm to 0.5 μm) of the pillars, Fig. 3a and 3b depict the transmitted phase and transmission coefficient of displacement as functions of pillar thickness and width, respectively. Two types of out-of-phase patterns with distinct transmission are observed at point A $t = 0.5$ μm, $w = 0.914$ μm and point B $t = 0.374$ μm, $w = 1.311$ μm, demonstrating high and low transmission efficiency, respectively. The geometrical parameters as point A are also used for the investigation of the pillar numbers. The two patterns occur very close to each other in the w-t plane, making it impossible to achieve efficient phase modulation only considering one geometric parameter. For example, when t=0.4 and w>0.8, the pillar resonance state transitions into the low transmission resonance mode B before fully exiting resonance mode A. This results in a smaller transmission coefficient in the phase interval of [0, 0.5].

To elucidate the different modes observed at points A and B, denoted by red dots in Fig. 3a and 3b, a frequency domain analysis around 600MHz was conducted. The transmitted scattering wave relative to the incident wave is defined as $w_s = \frac{w_p - w_{ref}}{w_{ref}}$, where w_p and w_{ref} are the out-of-plane displacement of the transmitted wave (with pillars) and the incident wave (without pillar) at detected point. In Fig.3c, The Nyquist plot of scattering wave w_s is displayed. The x-axis represents the real part of w_s, while the y-axis represents the imaginary part. Each point on the curves corresponds to the scattering response at a specific frequency. The distance from a point to the origin indicates the

amplitude of the scattering wave relative to the incident wave, and the angle between the line connecting the point to the origin and the x-axis represents the phase of the scattering wave relative to the incident wave. The metasurface units at points A (blue curve) and B (yellow curve) exhibit similar responses, depicting a spiral shape that contracts toward the center as the frequency increases, demonstrating the diversity of resonance modes. However, at the operating frequency of 600 MHz (purple box), the two points are in different resonance modes. In the Nyquist plot, the imaginary parts of the two points are nearly 0, and their real parts are negative, indicating that the scattered waves at both points are out-of-phase with respect to the incident wave. Specifically, the real parts of points A and B are about -1.8 and -1.47, which means that the amplitude of the out-of-phase scattered waves at the two points are 1.8 and 1.47 times of that of the incident wave, respectively. Considering destructive interference between the incident and scattering waves, the transmission is 0.8 and 0.47 for point A and B respectively, meanwhile both of them are out-of-phase. The geometric parameters with high transmission like point A will be selected for on-chip SAW metasurface design.
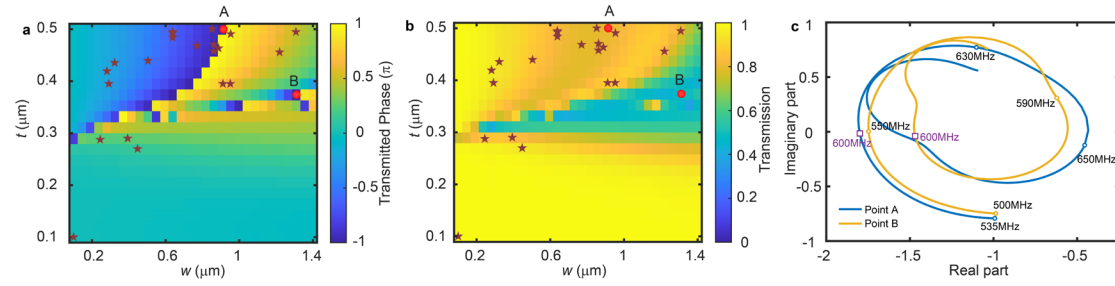

Fig.3 Variation of **(a)** transmitted phase and **(b)** transmission as a function of the thickness t and width w of pillars; red dots A and B represent two typical modes; red stars show the selected points for focusing metasurfaces. **c,** The Nyquist plot of scattering waves emitted by metasurfaces units at point A (blue curve) and B (yellow curve); The purple box represents the design frequency as 600MHz.

3. On-chip SAW metasurface design

The objective of this study is to design metasurfaces composed of distinct pillars capable of transforming an incident wave into desired wavefront patterns, including but not limited to splitting, beam deflection, focusing, and source illusion. Hereby, we concentrate on showcasing the focusing capability of the proposed metasurfaces, a functionality commonly employed for energy concentration and sensing. The plane wave focusing model can be designed based on the generalized Snell's law as demonstrated in Fig.4a. The metasurface comprises 41 units (marked as green), with the pillars in each unit varying in thickness and width to achieve different phase responses. A chirped interdigital transducer (IDT) is used to launch SAW in the experiment. To determine the phase of each unit, we have to start from the continuous phase response profile $\varphi(y)$ along the metasurface, which can be given by $\varphi(y) = \frac{2\pi}{\lambda}\left(\sqrt{F^2 + y^2} - F\right)$ where $\lambda = 6.7$ μm is the working wavelength, F is the focal length and y is the y-coordinate position along the metasurface. Since the metasurface is constructed from individual pillared units that cannot characterize continuous phase responses, it

becomes necessary to discretize the continuous phase based on the position of the units along the metasurface. Furthermore, given the anisotropic properties of the LiNbO$_3$ substrate, phase compensation caused by material is essential, operating on a discrete phase basis. Phase compensation of ith unit can be written as $\psi_i(y_i) = \frac{2\pi(\lambda-\lambda_i)}{\lambda\lambda_i}\sqrt{F^2 + y_i{}^2}$ where λ_i represents the wavelength of the SAW propagating at an angle of $\arctan(y_i/F)$ degrees to the x-coordinate. More details about phase compensation can be found in Supplementary materials. In Fig.4b, the continuous phase profile (green line) for $F = 2\lambda$ focusing is calculated and 41 discrete phase points (blue dots) are selected according to the unit positions. The choice of a small focal length is intended to better demonstrate the sub-wavelength focusing effect [20]. The final phases utilized for the metasurface units, after incorporating material phase compensation with discrete phases, is represented by the red stars. The significant discrepancy between the discrete phases and the metasurface phases underscores the importance of accounting for the effects of anisotropic materials.

Once the phase of metasurface units and the relationships between transmitted wave and geometric parameters of pillars are determined, the final step is to identify the optimal thickness and width of the pillars. Since we sweep both thickness and width, structures with the same phase can correspond to various geometric parameters. To achieve maximum efficiency, a fundamental principle involves selecting points with the highest transmission coefficients in Fig.3a and 3b that correspond to the target phase. The selected points are shown as red stars in Fig.3a and 3b, with an average transmission of 0.85, indicating sufficient energy in the focusing field. All the geometrical parameters of focusing metasurface can be found in Supplementary materials.
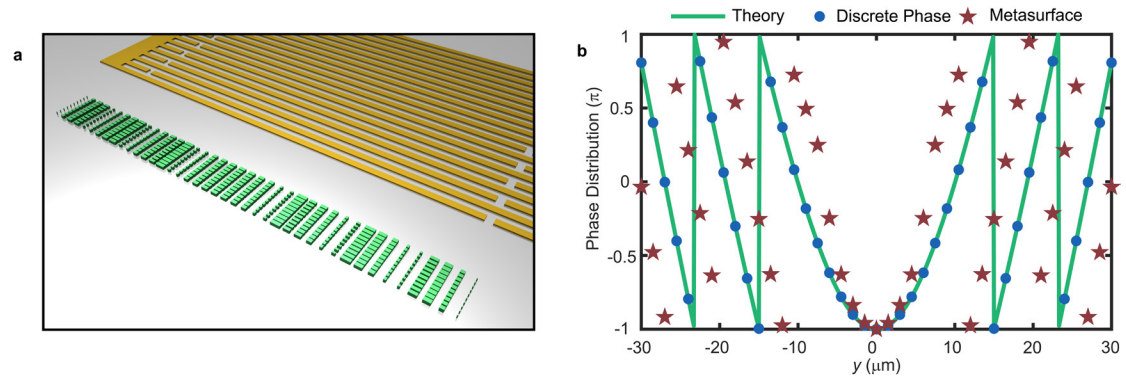

Fig.4 a, Demonstration of focusing model; green blocks are the on-chip SAW metasurface and yellow part denotes the IDT used for excitation; **b,** continuous phase profile (green line) for $F = 2\lambda$, discrete phases based on the position of each unit (blue dots) and final phase of metasurface units (red stars).

4. Device fabrication

The fabrication of the entire device can be divided into two stages: the preparation of the metasurfaces and the preparation of the IDT. Due to the material properties of niobium, combined with the hundred-nanometer structural scale and the high aspect ratio of the pillars, the fabrication of the on-chip SAW metasurface presents significant challenges. Fig. 5a to 5e illustrate our

fabrication process of the Nb pillars. Initially, a 450 nm Nb layer was deposited onto the cleaned wafer surface using sputtering with Plassys MP500. Patterns were then created using PMMA 672.03 resist through E-beam lithography (Raith Voyager). Subsequently, an evaporation of Cr for the plasma etching mask was carried out using Plassys MEB600, followed by a lift-off process to obtain the final mask. Plasma etching was conducted using Corial 200R to form the corresponding Nb pillars. Lastly, wet etching was employed to remove residual masks from the plasma etching process. The fabrication of the IDT follows a more standard process compared to the preparation of the Nb pillars. We utilized E-beam lithography with CSAR 18 resist to create the pattern, followed by the deposition of 100 nm Al electrodes through evaporation and lift-off steps. Chirped IDT properties can be found in Supplementary materials.
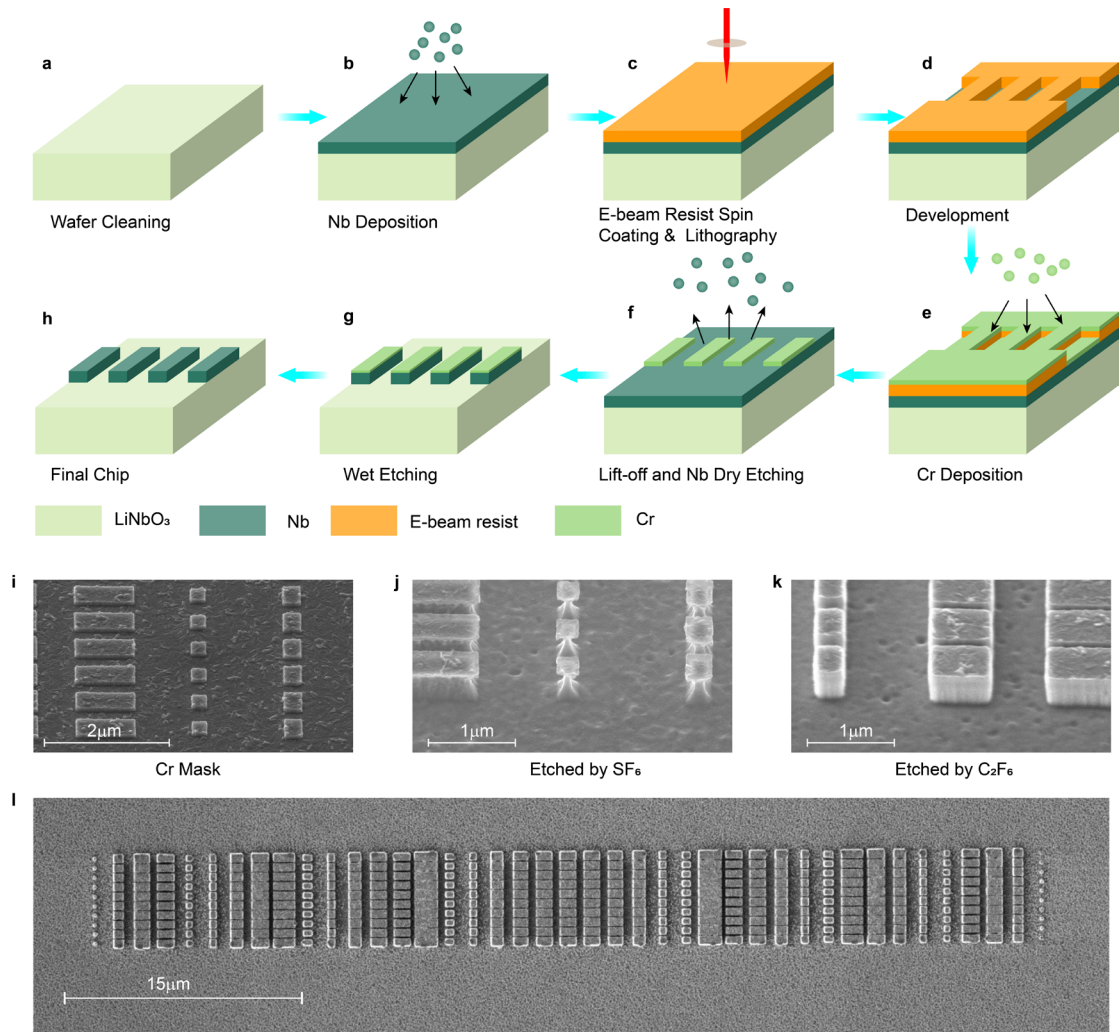
Fig.5 a~e, Illustration of the pillar fabrication process. **i**, Cr mask for plasma etching. (**j**) SF_6 and (**k**) C_2F_6 Etched pillars. **l,** top view of the focusing metasurface.

There are two key considerations during the fabrication process: 1) selecting the appropriate mask for plasma etching, and 2) configuration of the etching gases to achieve a vertical profile of the pillars. Due to the structures in the hundreds of nanometers range, high-precision E-beam lithography is essential, which limits the thickness of the deposition layers. Therefore, the material

must be sufficiently hard during dry etching to ensure the mask can be as thin as possible. Additionally, the mask should be easily removable using an Nb-insensitive wet etching solution. The Cr mask, as a plasma etching mask, perfectly meets the aforementioned conditions, as shown in Fig. 5i. The thickness of the Cr mask is only 65nm, which is only 14.4% of the pillar's height. Once the mask is determined, the attempt of plasma etching can be performed. Fig. 5j and Fig.5k show results of plasma etching using two based on different plasma gases: 25 sccm SF_6 (7 mTorr, 70 Watt) and 25 sccm C_2F_6 (with 5 sccm O_2 and 2 sccm Ar to increase the etch rate, 15 mTorr, 90Watt). In case of SF_6-based plasma etching (Fig. 5j) large under-etching in lateral direction occurred, possibly due to partial chemical etching of SF_6 plasma. Conversely, Fig. 5k displays a structure with desired vertical side walls, leading us to use C_2F_6 for the fabrication of devices. The final metasurface with 449 nm height is shown in Fig.5l.

5. Results

In the experiments, RF signals with a power level of 15 dBm are applied to the interdigital transducer to generate the surface acoustic wave. Subsequently, a heterodyne interferometric optical probe is used to scan the 25 µm × 25 µm focusing area located in front of the midpoint of the metasurface. The optical probe, out-of-plane acoustic field mapping measurement setup, is described in detail in the Supplementary Materials. At our design frequency of 600 MHz, the measured wavelength is 6.57 µm, which deviates by only 2% from the simulated wavelength. Despite this minor difference, simulated wavelength is utilized in all subsequent analyses. Fig. 6c and 6g display the amplitude fields from both simulation and experiment. Clearly discernible focusing spots in these figures provide strong evidence supporting the focusing capability of the SAW metasurface. The simulated focal length is 1.96λ, closely aligning with our designed focal length of 2λ as discussed in the metasurface design section and the experimentally measured focal length is 1.31λ. We attribute this discrepancy to several factors including variations in the material properties of niobium due to deposition conditions, imperfections in the shape of the pillars, and other factors potentially influencing the resonance states.

We also examined the broadband properties of these metasurfaces across a frequency range from 550 MHz to 650 MHz, achieving a frequency bandwidth ratio (bandwidth divided by the central frequency) of approximately 16.7%. For a more detailed comparison, we analyzed the size of the focal spot and focal length relative to the corresponding wavelength as a function of frequency. These comparisons are illustrated in upper (simulation) and lower (experiments) panels of Fig.6. Both the simulated and experimental focal lengths exhibit a slight increase with rising frequency, while the full width at half maximum (FWHM) along the *y*-direction gradually decreases, indicating a consistent trend between the experimental and simulated results. For a more visual comparison, the amplitude fields at frequencies of 550 MHz, 600 MHz, and 650 MHz are presented separately for both simulation and experiment in Fig. 6b to 6d and Fig. 6f to 6h. Notably, the maximum value indicated on the colorbar corresponds to the peak amplitude at the respective focal point. It is observed that the FWHM of the focal spot remains subwavelength in a broad band which is a remarkable feature of the on-chip SAW metasurface.
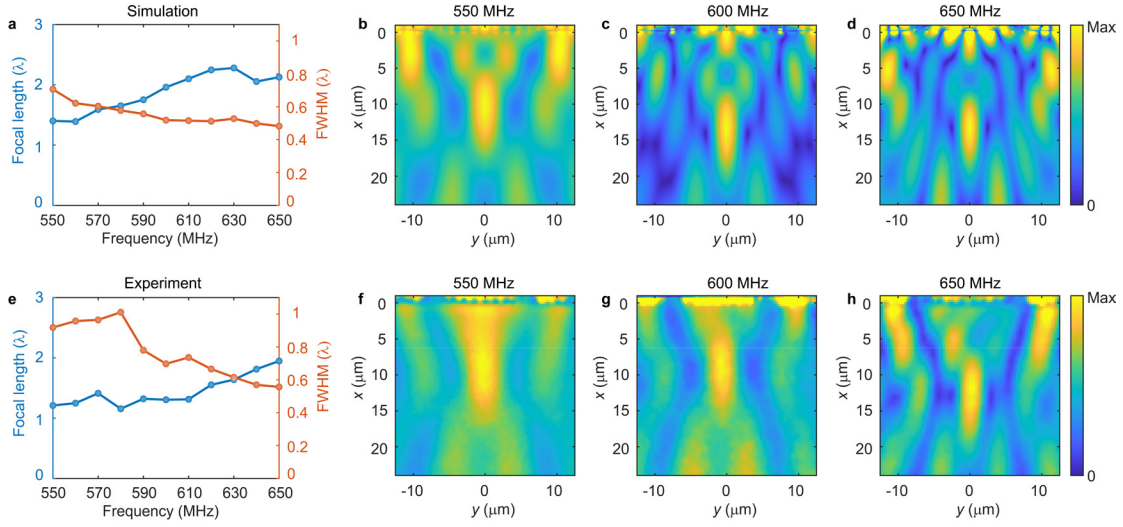
Fig.6 Variation of focal length (blue curve) and FWHM (red curve) along y-axis as a function of frequency in **(a)** simulation and **(e)** experiments. The amplitude fields at frequencies of **(b, f)** 550 MHz, **(c, g)** 600 MHz, and **(d, h)** 650 MHz. The first row displays the simulation results, while the second row presents the experimental findings.

6. Discussion

The overall results observed from this work suggest that a good focusing effect with broadband robustness can be achieved using different resonance modes of multiple submicron pillars. Notably, in addition to the focusing phenomenon, other wavefront modulations such as splitting and deflection can be easily achieved by employing different phase distribution functions. Here, we demonstrate a deflection case as an example. For a beam of normal incident SAW, achieving a deflection at an angle θ requires a phase distribution along metasurface given by $\varphi(y_i) = \frac{2\pi}{\lambda(\theta)} sin(\theta)y_i$ where $\lambda(\theta)$ is the new wavelength after deflection, and y_i denotes the position of the ith unit. The design angle 29.1° is chosen because the unit phases along the metasurface exhibit a periodic distribution, as shown in Fig. 7a. Consequently, by applying periodic boundary conditions, computational resources are optimized by focusing on a supercell comprising 8 subunits. The phases of these 8 subunits are indicated as red dots in Fig. 7a. In Fig. 7b, the real part of the out-of-plane displacement is presented, clearly demonstrating a deflection effect of approximately 31.4°.

Theoretically, this work extends the concept of elastic metasurfaces from the macroscopic scale to the submicron scale. The positive results obtained both theoretically and experimentally demonstrate the feasibility of the on-chip SAW metasurfaces for micro-nano scale chip and device applications. In terms of applications, specifically SAW manipulation, such metasurfaces offer advantages of simple structure and overall subwavelength size compared to conventional focused interdigital transducers or phononic crystals with periodic structures. Due to their compactness and passivity, these metasurfaces can be used in the future for directional manipulation of acoustic energy within quantum acoustic chips [21].
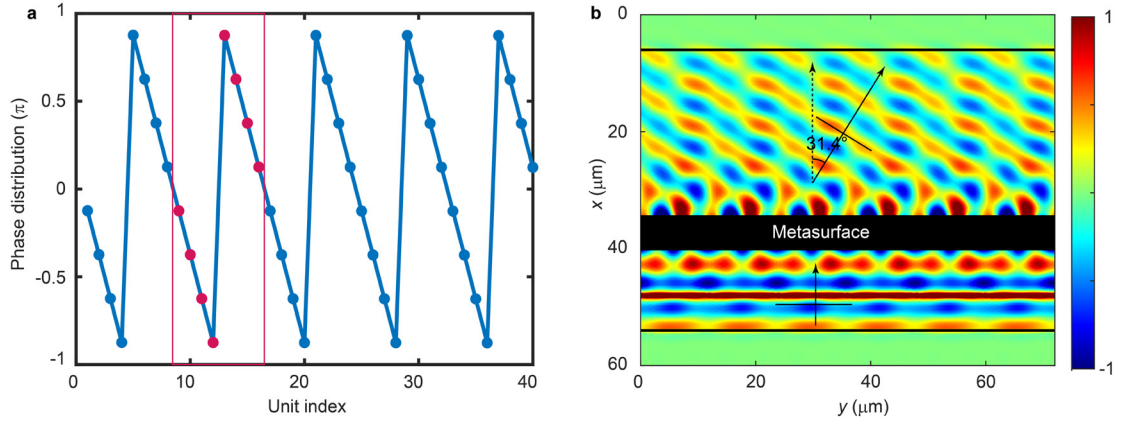
Fig. 7 a, Phase distribution along the metasurface, with red dots indicating the phases of subunits within a supercell. **b**, Real part of the out-of-plane displacement field illustrating the deflection.

7. Conclusion

In summary, we introduced theoretical and experimental realization of on-chip SAW metasurfaces composed of multiple pillared units designed for SAW manipulation. By analyzing the effects of scattered waves reemitted by the resonance modes of the units, we demonstrated that a 2π phase span with high transmission coefficients can be achieved by adjusting the width and thickness of the pillars. We illustrate this capability through the design of the SAW metasurface and show a microfabrication process for device preparation. Chromium is utilized as the etching mask, while C_2F_6 serves as an effective etching gas for niobium. The amplitude fields obtained from optical probe and simulations exhibit a strong agreement in trends, underscoring the broadband properties of such metasurfaces. Furthermore, these metasurfaces at micro-nanoscale can be adapted for various functions, including deflecting waves and splitting, offering significant potential for applications in MEMS, sensing, electronic chips, quantum devices, and beyond.

for IDT design.

Competing interests: The authors declare that they have no competing interests.

Data and materials availability: All data needed to evaluate the conclusions in the paper are present in the paper and/or the Supplementary Materials.

Reference

1. Kaina, N., et al., *Negative refractive index and acoustic superlens from multiple scattering in single negative metamaterials.* Nature, 2015. **525**(7567): p. 77-81.
2. Dubois, M., et al., *Observation of acoustic Dirac-like cone and double zero refractive index.* Nat Commun, 2017. **8**: p. 14871.
3. Zhang, Q., et al., *Gigahertz topological valley Hall effect in nanoelectromechanical phononic crystals.* Nature Electronics, 2022. **5**(3): p. 157-163.
4. Xue, H., Y. Yang, and B. Zhang, *Topological acoustics.* Nature Reviews Materials, 2022. **7**(12): p. 974-990.
5. Yu, N. and F. Capasso, *Flat optics with designer metasurfaces.* Nat Mater, 2014. **13**(2): p. 139-50.
6. Yu, N., et al., *Light propagation with phase discontinuities: generalized laws of reflection and refraction.* Science, 2011. **334**(6054): p. 333-7.
7. Kildishev, A.V., A. Boltasseva, and V.M. Shalaev, *Planar photonics with metasurfaces.* Science, 2013. **339**(6125): p. 1232009.
8. Taravati, S. and G.V. Eleftheriades, *Microwave Space-Time-Modulated Metasurfaces.* ACS Photonics, 2022. **9**(2): p. 305-318.
9. Glybovski, S.B., et al., *Metasurfaces: From microwaves to visible.* Physics Reports, 2016. **634**: p. 1-72.
10. Jin, Y., et al., *Flat acoustics with soft gradient-index metasurfaces.* Nat Commun, 2019. **10**(1): p. 143.
11. Xie, Y., et al., *Wavefront modulation and subwavelength diffractive acoustics with an acoustic metasurface.* Nat Commun, 2014. **5**(1): p. 5553.
12. Shen, Y.X., et al., *Ultrasonic super-oscillation wave-packets with an acoustic meta-lens.* Nat Commun, 2019. **10**(1): p. 3411.
13. Jin, Y., et al., *Physics of surface vibrational resonances: pillared phononic crystals, metamaterials, and metasurfaces.* Rep Prog Phys, 2021. **84**(8): p. 086502.
14. Assouar, B., et al., *Acoustic metasurfaces.* Nature Reviews Materials, 2018. **3**(12): p. 460-472.
15. Khorasaninejad, M., et al., *Metalenses at visible wavelengths: Diffraction-limited focusing and subwavelength resolution imaging.* Science, 2016. **352**(6290): p. 1190-4.
16. Chen, W.T., et al., *A broadband achromatic metalens for focusing and imaging in the visible.* Nat Nanotechnol, 2018. **13**(3): p. 220-226.
17. Liu, Y., et al., *Source Illusion Devices for Flexural Lamb Waves Using Elastic Metasurfaces.* Phys Rev Lett, 2017. **119**(3): p. 034301.
18. Zhu, H., et al., *Nonlocal elastic metasurfaces: Enabling broadband wave control via intentional nonlocality.* Proc Natl Acad Sci U S A, 2020. **117**(42): p. 26099-26108.
19. Lee, H., et al., *Mass-stiffness substructuring of an elastic metasurface for full transmission beam steering.* Journal of the Mechanics and Physics of Solids, 2018. **112**: p. 577-593.

20. Jin, Y.B., et al., *Elastic Metasurfaces for Deep and Robust Subwavelength Focusing and Imaging.* Physical Review Applied, 2021. **15**(2).

21. Delsing, P., et al., *The 2019 surface acoustic waves roadmap.* Journal of Physics D: Applied Physics, 2019. **52**(35): p. 353001.

22. Kim, Y., et al., *Chip-less wireless electronic skins by remote epitaxial freestanding compound semiconductors.* Science, 2022. **377**(6608): p. 859-869.

23. Gao, F., et al., *Acoustic radiation-free surface phononic crystal resonator for in-liquid low-noise gravimetric detection.* Microsystems & Nanoengineering, 2021. **7**(1): p. 10.

24. Ahmed, H., et al., *Acoustomicrofluidic assembly of oriented and simultaneously activated metal-organic frameworks.* Nature Communications, 2019. **10**: p. 9.

25. Zhang, Y. and Y. Yang, *Surface acoustic wave digital microfluidics with surface wettability gradient.* Lab Chip, 2024. **24**(13): p. 3226-3232.

26. Gustafsson, M.V., et al., *Local probing of propagating acoustic waves in a gigahertz echo chamber.* Nature Physics, 2012. **8**(4): p. 338-343.

27. Satzinger, K.J., et al., *Quantum control of surface acoustic-wave phonons.* Nature, 2018. **563**(7733): p. 661-665.

28. Shao, L., et al., *Non-reciprocal transmission of microwave acoustic waves in nonlinear parity–time symmetric resonators.* Nature Electronics, 2020. **3**(5): p. 267-272.

29. Zeng, Q., et al., *Milliseconds mixing in microfluidic channel using focused surface acoustic wave.* Sensors and Actuators B-Chemical, 2011. **160**(1): p. 1552-1556.

30. Nam, J., W.S. Jang, and C.S. Lim, *Micromixing using a conductive liquid-based focused surface acoustic wave (CL-FSAW).* Sensors and Actuators B-Chemical, 2018. **258**: p. 991-997.

31. Ma, Z., et al., *Generating Airy surface acoustic waves with dislocated interdigital transducers.* Lab Chip, 2024. **24**(20): p. 4808-4815.

32. Gao, F., et al., *On-Chip Tightly Confined Guiding and Splitting of Surface Acoustic Waves Using Line Defects in Phononic Crystals.* Advanced Functional Materials, 2023.

33. Wang, J.Q., et al., *Extended topological valley-locked surface acoustic waves.* Nat Commun, 2022. **13**(1): p. 1324.

34. Sun, J.-H. and Y.-H. Yu, *Anisotropic surface acoustic waves in tungsten/lithium niobate phononic crystals.* Applied Physics A, 2018. **124**(2).

35. Zhao, J., et al., *Focusing of Rayleigh waves with gradient-index phononic crystals.* Applied Physics Letters, 2016. **108**(22).

36. Jin, Y., B. Djafari-Rouhani, and D. Torrent, *Gradient index phononic crystals and metamaterials.* Nanophotonics, 2019. **8**(5): p. 685-701.

37. Wu, X., et al., *Broadband Rayleigh wave attenuation by gradient metamaterials.* International Journal of Mechanical Sciences, 2021. **205**.

38. Cai, R., et al., *Attenuation of Rayleigh and pseudo surface waves in saturated soil by seismic metamaterials.* Computers and Geotechnics, 2024. **165**.

39. Chen, A.L., H.-W. Zhang, and Y.-S. Wang, *Flexible wavefront modulation of Rayleigh surface waves by mechanically reconfigurable elastic metasurface.* Extreme Mechanics Letters, 2023. **64**.

40. Harley, W.S., et al., *3D acoustofluidics via sub-wavelength micro-resonators.* Advanced Functional Materials, 2023. **33**(9): p. 2211422.

41. Xu, M., P.V.S. Lee, and D.J. Collins, *Microfluidic acoustic sawtooth metasurfaces for patterning and separation using traveling surface acoustic waves.* Lab Chip, 2021. **22**(1): p. 90-99.

42. Yeo, L.Y. and J.R. Friend, *Surface acoustic wave microfluidics.* Annual review of fluid mechanics, 2014. **46**(1): p. 379-406.

43. Pennec, Y., et al., *Low-frequency gaps in a phononic crystal constituted of cylindrical dots deposited on a thin homogeneous plate.* Physical Review B, 2008. **78**(10).

44. Wu, T.-C., T.-T. Wu, and J.-C. Hsu, *Waveguiding and frequency selection of Lamb waves in a plate with a periodic stubbed surface.* Physical Review B, 2009. **79**(10).

45. Chen, W.T., A.Y. Zhu, and F. Capasso, *Flat optics with dispersion-engineered metasurfaces.* Nature Reviews Materials, 2020. **5**(8): p. 604-620.

46. Aieta, F., et al., *Aberration-free ultrathin flat lenses and axicons at telecom wavelengths based on plasmonic metasurfaces.* Nano Lett, 2012. **12**(9): p. 4932-6.

47. Jin, Y., et al., *Pillar-type acoustic metasurface.* Physical Review B, 2017. **96**(10): p. 104311.

Supplementary materials

Experimental realization of on-chip surface acoustic wave metasurfaces at sub-GHz

Wan Wang[1,2], Maciej Baranski[2], Yabin Jin[3,4,*], Roland Salut[2], Djaffar Belharet[2], Jean-Michel Friedt[2], Yongdong Pan[1], Yanxun Xiang[3], Fu-zhen Xuan[3], Abdelkrim Khelif[2], Sarah Benchabane[2,*]

[1]School of Aerospace Engineering and Applied Mechanics, Tongji University, 200092 Shanghai, China

[2]Université de Franche-Comté, CNRS, FEMTO-ST, 15B avenue des Montboucons F-25000 Besançon, France

[3]Shanghai Key Laboratory of Intelligent Sensing and Detection Technology, School of Mechanical and Power Engineering, East China University of Science and Technology, 200237 Shanghai, China

[4]Shanghai Institute of Aircraft Mechanics and Control, 200092 Shanghai, China

[*]Corresponding author: yabin.jin@ecust.edu.cn; sarah.benchabane@femto-st.fr

1. Numerical simulations.

All simulations were conducted using the Finite Element Method through frequency domain calculations in COMSOL. Considering the piezoelectric effect of lithium niobate, we employed the Solid Mechanics and Electrostatics modules for substrate calculations, while the niobium pillars were solely analyzed using the Solid Mechanics module. An out-of-plane line force was applied to the substrate surface to excite surface acoustic waves. For unit simulations, perfectly matched layers (PML) are positioned at the wave propagation end and the substrate bottom to minimize wave reflection. Periodic boundary conditions were implemented on the substrate side perpendicular to the wave propagation direction to simulate infinite units. For the focusing model, PML are employed to minimize boundary effects, while symmetry conditions are applied to reduce computational time and resources.

2. Metasurface units for different numbers of pillars.

The primary consideration in selecting the number of pillars is the transmission efficiency while achieving out-of-phase function. Fig. S1 illustrates the variation of the transmitted phase and transmission as a function of the number of pillars. The calculations for this figure were based on the same geometrical parameters as point A in Fig.3a. It is worth noting that structures with fewer than 10 pillars are not in the strongest resonance state (i.e., have not achieved out-of-phase). Consequently, their transmission, when attempting to realize out-of-phase, will be significantly weaker than in the current configuration. This result evident that with around 10 pillars, the highest transmission can be achieved, while also realizing the out-of-phase phenomenon. Another secondary consideration is minimizing the overall size of the metasurface to fully leverage its

subwavelength compactness. Considering all factors, the gain in transmittance efficiency from further increasing the number of pillars becomes negligible, which is why values exceeding 10 such as 11 were not considered.
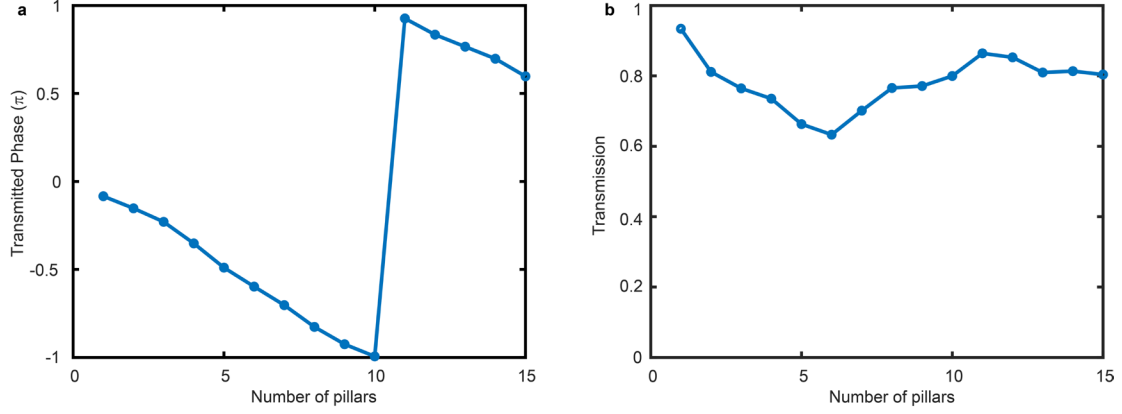

Fig.S1 Variation of (a) transmitted phase and (b) transmission as a function of the number of pillars with the same geometrical parameters as point A in Fig.3a.

3. Phase compensation caused by anisotropic material properties

As an anisotropic material, lithium niobate exhibits distinct surface acoustic wave velocities in different directions. In the context of plane wave focusing, the variation in refractive index causes a shift in the propagation direction of the plane wave as it passes through the metasurface, resulting in a change in the wave velocity that must be carefully considered. Since the wavelength can be directly related to the wave velocity, we present the FEM model used to calculate the wavelength at 600 MHz in different directions in Fig.S2. Due to the symmetry of the material properties of lithium niobate, a quarter of the cylinder is used for wavelength calculations to conserve computational resources. Perfectly matched layers are applied to the outer and bottom domains of the cylinder to minimize boundary reflections. Symmetry conditions are applied to the cut surface of the quarter-cylinder to simulate a full-angle scenario. A point source is positioned at the center of top surface of the cylinder to excite the circular SAWs. Two probe lines, line 1 and line 2, are placed at distances of $5\lambda_0$ and $7\lambda_0$ from the point source, where λ_0 represents the wavelength of propagation along the x-direction at 600 MHz.
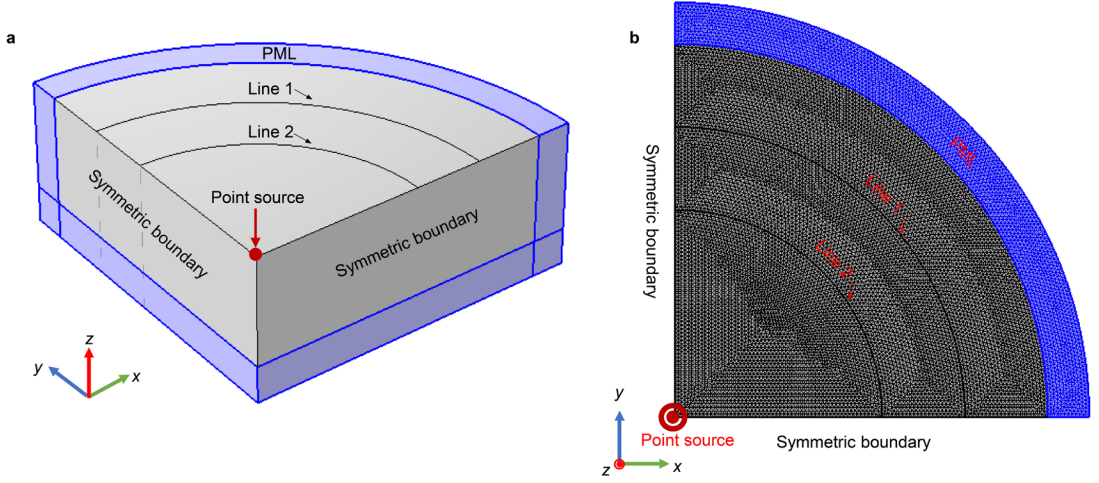
Fig.S2 (a) Axonometric view and (b) top views of the model used to calculate the wavelength of lithium niobate in different directions.

The out-of-plane displacements obtained at the two probe lines are denoted as w_1 and w_2 respectively. The unit phase difference between the two probe lines can be written as

$$\Phi(\theta) = \arg\left(\frac{w_2(\theta)}{w_1(\theta)}\right)/2\lambda_0 \tag{1}$$

where θ is the angle with the x-direction. Further, the wavelength can be written:

$$\lambda(\theta) = 2\pi/(\Phi(\theta) + 2\pi/\lambda_0) \tag{2}$$

The result of $\lambda(\theta)$ can be found in Fig.S3. Once the wavelengths at each angle are determined, the compensating phase can be calculated. The angle of ith unit of metasurfaces is

$$\theta_i = \arctan(y_i/F) \tag{3}$$

where y_i is the location of the unit, and F is the focal length. The distance between ith unit and the focal point is

$$L_i = \sqrt{y_i^2 + F^2} \tag{4}$$

The phase compensation caused by unit distance can be written as

$$\eta_i = \frac{2\pi}{\lambda(\theta_i)} - \frac{2\pi}{\lambda_0} \tag{5}$$

Thus, phase compensation of ith unit of metasurfaces can be written as

$$\psi_i(y_i) = \eta_i L_i = \frac{2\pi(\lambda_0 - \lambda(\theta_i))}{\lambda_0 \lambda(\theta_i)}\sqrt{F^2 + y_i^2} \tag{6}$$

The final phases of metasurface units are

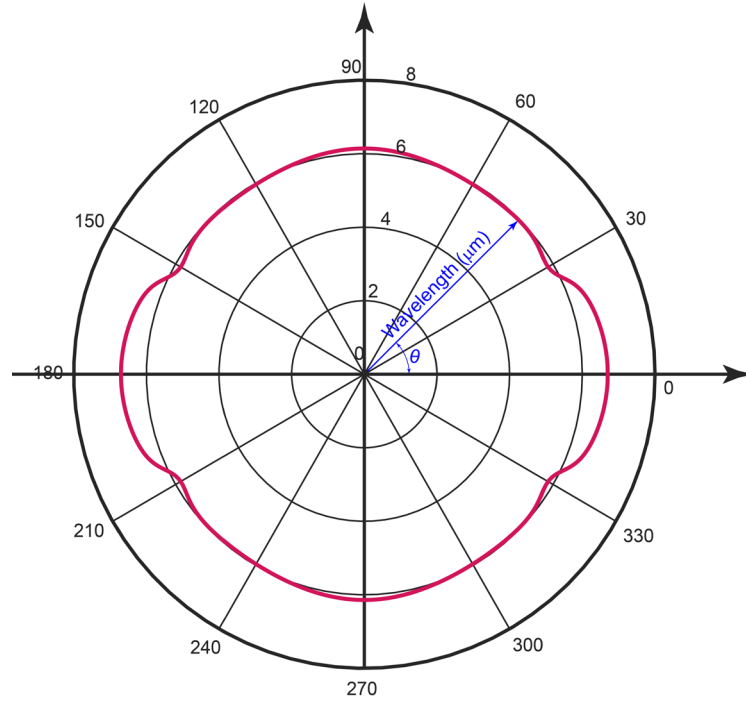$$\varphi(y_i) = \frac{2\pi}{\lambda}\left(\sqrt{F^2 + y_i^2} - F\right) - \psi_i(y_i) \tag{7}$$

Fig.S3 Wavelength variation diagram of lithium niobate at different angles with respect to the x-direction.

4. Geometrical parameters of focusing metasurface

The specific geometric parameters of the metasurface used for focusing surface acoustic waves (SAWs), including thickness (t) and width (w), are listed below.

Table S1 Geometrical parameters of focusing metasurface

i-th unit	w (μm)	t (μm)
1	0.100	0.100
2	0.504	0.439
3	0.852	0.500
4	0.952	0.395
5	0.244	0.287
6	0.281	0.419
7	0.638	0.484
8	0.954	0.491
9	1.220	0.456
10	0.447	0.270
11	0.323	0.435
12	0.638	0.495
13	0.862	0.458
14	0.911	0.395
15	1.308	0.495

16	0.394	0.290
17	0.292	0.395
18	0.638	0.493
19	0.770	0.468
20	0.862	0.470
21	0.888	0.463
22	0.862	0.470
23	0.770	0.468
24	0.638	0.493
25	0.292	0.395
26	0.394	0.290
27	1.308	0.495
28	0.911	0.395
29	0.862	0.458
30	0.638	0.495
31	0.323	0.435
32	0.447	0.270
33	1.220	0.456
34	0.954	0.491
35	0.638	0.484
36	0.281	0.419
37	0.244	0.287
38	0.952	0.395
39	0.852	0.500
40	0.504	0.439
41	0.100	0.100

5. Chirped IDT properties

In this work, to test the broadband performance of metasurfaces, a broadband excitation method is required. The chirped IDT provides an excellent solution through its gradient electrode width and spacing distribution which is based on the working frequency. Our IDT consists of a total of 74 electrode pairs with an aperture of 63.5 μm. In Fig. S4a, the variation of pitch and metallization ratio with electrode pair indexing is presented, exhibiting a linear trend. In Fig. S4b, we present the experimentally measured values of |S11|, which characterize the intensity of the reflection of the input electrical signal. A smaller value of |S11| indicates a greater conversion of electrical energy into mechanical energy (SAW), corresponding to a higher level of excitation. A value of |S11| equal to 0 indicates that the electrical signal is fully reflected, and no surface acoustic wave is excited. The results in Fig. S4b demonstrate the broadband operating performance of the IDT, especially from 550MHz to 650 MHz. For this work, we only need to excite SAW at the appropriate frequency,

without requiring particularly high intensity, as long as they are strong enough to be detected by optical probe. Therefore, impedance optimization for higher intensity excitation was not performed.
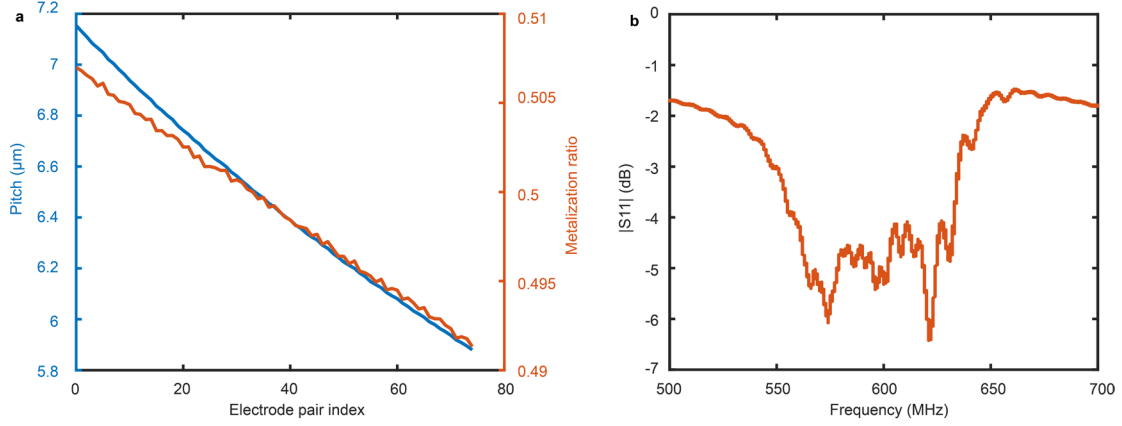

Fig.S4 (a) Variation of pitch (blue curve) and metallization ratio (red curve) with index of electrode pair; (b) Measured |S11| response of our chirped IDT.

6. Optical characterization.

The 25 μm × 25 μm scanning area is shown in Fig.S5a. An analog signal generator, Agilent N5181A, was employed to drive the interdigital transducer at a single frequency for each test, with the drive power consistently set at 15 dBm. Out-of-plane displacement fields were measured using a laser scanning heterodyne interferometer, with measurement steps of 0.25 μm (550 MHz, 560 MHz) or 0.3 μm (from 570 MHz to 650 MHz). As shown in Fig.S5b, laser beam from frequency stabilized HeNe ($\lambda = 633$ nm) source (Thorlabs HRS015B) is split into two frequency-shifted paths using an acousto-optic modulator driven at 110 MHz (AA Opto Electronic MTS110-A3-VIS). The first frequency-shifted beam served as a reference and was sent to a polarizing beam splitter. In contrast, the second beam propagated through a half-wave plate, the same polarizing beam splitter, a quarter-wave plate, and finally reached the substrate surface. A 0.6 μm spot focusing of the laser beam was achieved using a microscope objective (Olympus LMPLFLN100x). Upon reaching the sample, the laser beam returned, passing through the quarter-wave plate for a second time to rotate its polarization, which makes this beam to be reflected by the beam splitter and recombined with first beam. The combined beams were then directed to a fast photodiode (Alphalas UPD-200-SP) after passing through a linear polarizer. Finally, the electric signal captured by the photodiode was routed to an electrical spectrum analyzer (Anritsu MS2830A) for amplitude measurements or to an oscilloscope (Agilent DSO9254A) for phase measurements.
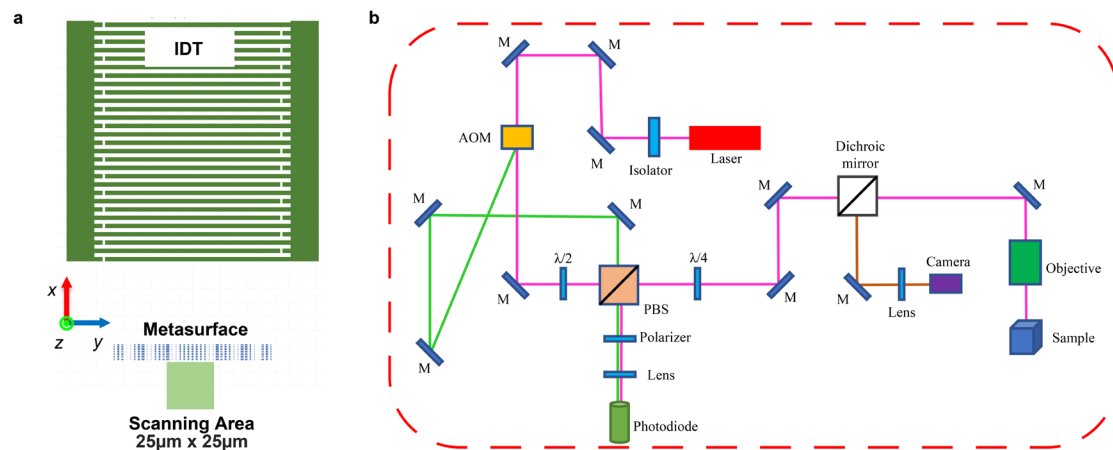
Fig. S5 Demonstration of (**a**) scanning area and (**b**) optical probe.